Enhanced photo-piezo-catalytic properties of Co-doped $Ba_{0.85}Ca_{0.15}Zr_{0.1}(Ti_{1-x}Co_x)_{0.9}$ ferroelectric ceramics for dye degradation

Yan Zhao[a], Qianqian Xu[a], Xuefan Zhou [a, *], Mingyang Yan[a], Hanyu Gong[a], Xi Yuan[b], Hang Luo[a], Kechao Zhou[a], Dou Zhang[a], Chris Bowen[c], Yan Zhang[a, *]

[a] *State Key Laboratory of Powder Metallurgy, Central South University, Changsha, Hunan 410000, China*

[b] *College of Chemistry and Chemical Engineering, Central South University, Changsha, Hunan 410000, China*

[c] *Department of Mechanical Engineering, University of Bath, Bath BA2 7AY, UK*

Abstract

This paper provides a detailed evaluation of the photo-piezo-catalytic properties of $Ba_{0.85}Ca_{0.15}Zr_{0.1}(Ti_{1-x}Co_x)_{0.9}$(BCZT-*x*Co,*x* = 0 - 0.025) ferroelectric ceramics prepared by a solid-state process. By control of the Co doping level, the band gap was reduced to 2.40 eV at the composition *x* = 0.02, which improved the generation of photo-generated charges and enhanced the photocatalytic activity. When a solution containing BCZT-0.02Co particles under both ultrasound and illumination, the degree of degradation of Rhodamine B reached 99% within 60 min, which was greater than when subjected to illumination or ultrasound alone. The examination of the dielectric properties, photoelectrochemical measurements and band energy structure of the materials provided new insights into the catalytic mechanism, where a strong coupling between piezoelectricity and photoexcitation was clearly observed. This work therefore highlights the attractive photo-piezo-catalytic properties of BCZT-*x*Co doped ceramics and is the first demonstration that Co substitution in these lead-free ferroelectric ceramics provides significant potential for photo-piezo-catalysis applications.

* Corresponding author at: State Key Laboratory of Powder Metallurgy, Central South University, Changsha, Hunan 410000, China.
E-mail address: yanzhangcsu@csu.edu.cn *(Y. Zhang)* *zhouxuefan@csu.edu.cn (X. Zhou)*

Keywords

Barium calcium zirconate titanate ceramics, doping modification, band gap decreasing, photo-piezo-catalysis

1. Introduction

Photocatalysis represents an ecofriendly and efficient technology for contamination remediation, and has therefore received widespread interest in response to global challenges in energy and environmental pollution [1, 2]. However, the performance of existing photocatalytic materials is often limited due to the recombination of photoexcited charge carriers[3]. Recently, significant effort has been made to facilitate the separation of carriers and reduce recombination rates using a variety of methods, which include impurity doping[4, 5], noble metal modification[6] and the construction of a heterojunction[7, 8]. Nevertheless, the efficiency continues to be limited in many cases.

On this basis, Wang *et al*. recently proposed the concept of *piezo-phototronics*, which combines the piezoelectric polarization and semiconductor properties of a material to manipulate charge transport and charge separation[9]. Piezoelectric materials are able to generate a built-in electric field under an applied mechanical stress to promote carrier separation[10] and tune the band structure to facilitate reduction – oxidation (redox) reactions[11, 12],which in turn facilitate catalysis. This process is not only able to harvest light (solar energy) but can also capture environmental mechanical energy[13]. Among the range of available piezoelectric materials, the lead zirconate titanate (PZT) family has been widely used as a result of its outstanding piezoelectric properties. However, due to the high toxicity of lead (Pb)[14, 15], there is an urgent need to develop environmentally lead-free piezoelectric materials that can compete with lead-based PZT materials for a range of applications[16, 17]. Several lead-free materials, which include

$Ba_{0.7}Sr_{0.3}TiO_3$ particles[18], ZnO nanorods[19], $BaTiO_3$ pellets[20], $BaZr_{0.02}Ti_{0.98}O_3$ powders[21], $K_{0.5}Na_{0.5}NbO_3$ particles[22], and $Ba_{1-x}Ca_xTiO_3$ nanowires[23] have been shown to demonstrate a coupling between mechanical, electrical, and chemical fields, leading to an increased efficiency in the degradation of pollutants. As a classical perovskite ferroelectric, ceramics based on the $BaTiO_3$-based system are one of the most extensively studied lead-free piezoelectric materials. In 2009, Liu *et al.* reported on a Ca and Zr co-doped $BaTiO_3$-based system, $0.5Ba(Zr_{0.2}Ti_{0.8})O_3–0.5(Ba_{0.7}Ca_{0.3})TiO_3$ (BCZT) whose composition was at a tri-critical point-type morphotropic phase boundary (MPB), which exhibited an extremely high piezoelectric constant d_{33} (~620 pC/N) and could achieve properties comparable to leading PZT materials[24]. As a result, the $Ba_{0.85}Ca_{0.15}Ti_{0.9}Zr_{0.1}O_3$ (BCZT) system is of interest as an environmentally friendly catalysts due to its relatively high piezoelectric coefficient[24], lead-free nature[25] and high saturation polarization (17 $\mu C/cm^2$)[26]. However, as is observed for many traditional ferroelectric materials[27], the band gap of BCZT is relatively large (3.18 eV) which limits the spectrum of photons that can be harvested to create electron–hole pairs under the application of ultra-violet (UV) light [28]. A reduction in the band gap of the BCZT system to coincide with the visible spectrum is therefore one of the emerging strategies to create photo-active materials; this is achieved using composite semiconductors[29], metal loading[30] and doping[31]. The first two methods are relatively time-consuming and high-cost, while doping is a facile and effective method which has attracted widespread attention [32]. Compared with pure BCZT, doped BCZT has the potential to create vacancy defects and reduce the effective band gap to achieve visible light photocatalytic activity [33]. Zhang *et al.* reported that transition metal (TM) doped BCZT lead-free ceramics, where TM = Mn, Fe, Co, and Ni, which were able to enhance the optical properties. The band gaps of BCZT - 0.05Mn, BCZT - 0.05Fe, BCZT - 0.05Co, and BCZT - 0.05Ni are 1.95, 2.26, 1.68, and 3.04 eV, respectively, which are considerably lower than that of the pure BCZT (3.18

eV)[28]. Among them, the band gap of Co-doped BCZT with is lower than many other perovskite ceramics[34], however, no detailed exploration of the photo-piezo-catalytic performance evaluation of BCZT-Co ceramics has been provided to date.

This work therefore provides the first evaluation of the photo-piezo-catalytic capability of $Ba_{0.85}Ca_{0.15}Zr_{0.1}(Ti_{1-x}Co_x)_{0.9}$ (BCZT - *x*Co, x = 0 - 0.025) ferroelectric ceramics. Cobalt was introduced to the BCZT system to form a series of $Ba_{0.85}Ca_{0.15}Zr_{0.1}(Ti_{1-x}Co_x)_{0.9}$ (x = 0, 0.01 ,0.015, 0.02 and 0.025) ferroelectric ceramics and the dielectric properties, optical properties, and catalytic performance are examined in detail to reveal the underlying mechanisms for dye degradation applications.

2. Experimental

2.1. Preparation of BCZT - *x*Co powder and pellets

The $Ba_{0.85}Ca_{0.15}Zr_{0.1}(Ti_{1-x}Co_x)_{0.9}$ (x = 0, 0.01, 0.015, 0.02 and 0.025) powders and pellets used in this work were prepared by a conventional solid-state process. All chemicals and reagents were obtained commercially and used without further purification. Analytical grade $BaCO_3$ (99%), $CaCO_3$ (99%), TiO_2 (99%), ZrO_2 (99%) and CoO (AR) were used as raw materials. The raw powders were weighed according to the required stoichiometric rations. Subsequently, the powders were ball-milled for 24 h, with alcohol being used as the milling agent.

For photoelectrochemical and catalytic characterisation, the balled-milled powders milling were calcined at 1350°C for 3 h. To produce dense materials for electrical measurements, 1.5 g aqueous solution of polyvinyl (5wt %) was mixed in 5g calcinated powder of BCZT - *x*Co and pressed into circular pellets with a 12 mm diameter and 1.0 mm thickness. Dense BCZT - *x*Co pellets were then obtained after sintering in a furnace at 1350°C for 3 h.

2.2. Characterization and measurements

The phase structure of the BCZTO - *x*Co powders were evaluated by an X-ray diffraction technique (XRD, PAN-analytical Empyrean, Netherlands) in the range of 20° and 80°. Scanning electron microscopy (SEM, Ultim Max 40, tescan mira4 LMH) was used to characterize the morphology. Polarization - electric field (*P*-*E*) ferroelectric hysteresis loops were characterized using a TF Analyzer 2000 (aixACCT systems, Germany). BCZT-xCo pellets were poled at an electric field of 3 kV/mm at 60°C in a silicone oil bath for 30min. The d_{33} piezoelectric charge coefficient of poled pellets was measured by a piezoelectric d_{33} meter (ZJ-4AN, Institute of Acoustics, Academic Sinica, China). A spectrophotometer (UV-2450, Shimadzu, Japan) was used to record the UV-Vis spectra of the materials and the UV–vis absorbance spectra of the solution were obtained via a UV–vis spectrometer (UV-2000i, Shimadzu, Japan).

2.3. Catalytic performance

The photocatalytic, piezocatalytic and photo-piezo-catalytic activity of the BCZT - *x*Co materials were measured by the decomposition of Rhodamine B (RhB) dye solutions. An ultrasonic source (200 W, 45/80/100kHz, KQ-200VDE, China) and a 300 W Xe lamp (PLS-SXE300D, Perfect Light, China) was selected to provide a periodic mechanical load and simulated sunlight source, respectively. In a typical process, 100 mg of the ceramic powder was dispersed into 100 ml of RhB aqueous solution (initial concentration C_0 = 10 mg/L) in a 200mL beaker. The solution was then stirred for 45 min in the dark to establish adsorption-desorption equilibrium between the dye and the catalysts. A 6 ml reaction solution was collected every 15 min during ultrasonic treatment and/or illumination irradiation and the supernatant was analyzed by the UV–vis spectrometer to record the change in dye absorbance. ESR measurements were also performed for radical confirmation and 5, 5-dimethyl-1-pyrroline N-oxide (DMPO) was used as a spin

trap. Typically, a 5mg/mL catalyst solution was prepared where the deionized water and Dimethyl Sulfoxide (DMSO) were used as solvents for the ESR detection of ·OH and $\cdot O_2^-$, respectively. After 20 min of illumination irradiation and/or ultrasonic treatment, 50 μL of the solution was taken out and mixed with 5 μL of DMPO, then encapsulated in a glass capillary tube for ESR test on Bruker model A300 spectrometer (Bruker A300, Germany).

2.4. Photoelectrochemical measurements

Photoelectrochemical experiments were performed in a standard three electrode electrochemical work station (Chenhua CHI604E, Shanghai). A platinum foil and Ag/AgCl electrode was used as the counter and reference electrodes, respectively, with a 0.5 mol/L Na_2SO_4 aqueous solution as the electrolyte. The working electrode was prepared as follows: 20 mg of catalyst and 50 μL of Nafion aqueous solution were dispersed in 2 mL ethyl alcohol, followed by sonication for 30 min. Subsequently, 60 μL suspension was coated onto the surface of a fluorine doped tin oxide (FTO) conducting glass (coated area: 1×1 cm^2) and annealed at 200 ◦C for 3 h. The setup was illuminated with visible light using a 300 W Xe lamp (PLS-SXE300, Perfect Light, China). Photocurrent-potential (*J* - *V*) curves under alternating light and dark were recorded by linear sweep voltammetry (LSV). Mott-Schottky tests were measured at different frequency of 1 kHz, 2 kHz and 3 kHz, respectively.

3. Results and discussions

3.1. Characterization of catalyst

Figure 1(a) shows an X-ray photoelectron spectroscopy (XPS) spectrum of Co 2p and Ba 3d for the BCZT - 0.02Co material. In the range of 775–800.5 eV, the peaks of Co $2p_{3/2}$ and Ba $3d_{5/2}$ and the peaks of Co $2p_{1/2}$ and Ba $3d_{3/2}$ overlap at approximately 777.8 eV and 793.3 eV, respectively[33]. The spectrum is

deconvoluted into three components. The binding energies for Ba $3d_{3/2}$ and Ba $3d_{5/2}$ are located at 793.95 eV and 779.6 eV, respectively, which can be assigned to Ba^{2+}[35]. The two peaks centered at 780.21 eV and 795.51 eV arise from the Co^{2+} $2p_{3/2}$ and Co^{2+} $2p_{1/2}$, indicating the presence of Co^{2+}[33]. Notably, the peaks present at 793.3 and 777.8 eV are assigned to Co^{3+} $2p_{1/2}$ and Co^{3+} $2p_{3/2}$, which indicates the existence of Co^{3+}[35]. Co^{2+} is partially oxidized to Co^{3+} when the CoO-doped BCZT was sintered under atmospheric conditions. However, the concentration of Co^{3+} is relatively lower in comparison to that of Co^{2+} since the Co^{2+} is typically more stable than Co^{3+}[36].

Figure 1(b) shows the XRD pattern in the range of 20°–80°for the BCZT - *x*Co powders at Co additions of x = 0 - 0.025. As seen in Figure 1(b), it can be seen that all peaks are well matched with the pure perovskite structure after sintering at 1350°C for 3 h[37]; this demonstrates that stable solid solutions are formed after the introduction of Co into the BCZT structure. The Co ions replace and occupy the Zr^{4+} or Ti^{4+} ion positions since the ionic radii of Co^{2+} (0.665 Å) and Co^{3+} (0.61 Å) are close to that of Ti^{4+} (0.605 Å) and Zr^{4+} (0.72 Å)[38]. Figure 1(c) shows fine-scale scanned XRD patterns at approximately $2\theta = 45°$ for the BCZT - *x*Co ceramics. For the pure BCZT ceramic, without any Co-doping, a coexistence of rhombohedral (*R, R3m*, PDF#85-1797) and tetragonal (*T, P4mm*, PDF#05-0626) phases was observed. With the introduction of Co by doping, the (200) peaks were weakened, indicating a phase transformation from the tetragonal phase to the rhombohedral phase, leading to only the rhombohedral phase being detected in the BCZT - *x*Co ceramics. After 24h of ball-milling, the morphology and particle size of the powders are highly uniform and exhibit a tight size distribution, as shown in Figure S1.

Figure 1(d-h) show scanning electron microscopy (SEM) images of the surface morphology of the sintered BCZT - *x*Co (x = 0, 0.01, 0.015, 0.02, and 0.025) pellets. All samples exhibit a dense structure and the grain size was calculated based on surface morphologies using ImageJ software. For the pure BCZT

material, a relatively large average grain size of ~15.2 μm and clear grain boundaries were obtained. The average grain size of BCZT - *x*Co ceramics were ~12.5, 10.3, 7.1, and 4.8 μm for compositions $x = 0.01$, 0.015, 0.020, and 0.025, respectively. Grain refinement occurs on Co-doping since the kinetic energy needed for the nucleation growth of Co-doped ceramics was low[39]. Furthermore, the atomic weight of Co ion is higher than that of Ti^{2+} and Zr^{2+}, leading to a low mobility of the Co ion, which accounts for a decrease in grain size with an increase in Co content[40]. Similar growth mechanisms have also been observed in Fe-doped $Ba_{0.85}Ca_{0.15}Zr_{0.1}(Ti_{1-x}Co_x)_{0.9}$[13], Co-doped $BaTiO_3$[41], and Ni-doped $PbTiO_3$[42].

3.2. Dielectric properties and optical properties of catalyst

Figure 2 shows the polarisation-electric field (*P*-*E*) hysteresis loops, remnant polarization (P_r) and piezoelectric coefficient (d_{33}) of the BCZTO - *x*Co ceramics at room temperature for different Co additions from $x = 0$ to $x = 0.025$. At an electric field of 3 kV/mm and 1 Hz, all the *P*-*E* ferroelectric hysteresis loops were slim with good rectangularity, confirming the good ferroelectric response of the BCZT – *x*Co materials. As shown in Figure 2(b), with an increase in Co content, the P_r and d_{33} decreased from $P_r = 11.53$ μC/cm^2 to $P_r = 2.05$ μC/cm^2, and $d_{33} = 307$ pC/N to $d_{33} = 139.3$pC/N, respectively, indicating a hard doping effect through the formation of a defect dipole pair with doping level[43].

To determine the optical properties of the BCZT – *x*Co materials, the bandgap was estimated using Tauc's plots[44]. The UV–vis absorbance spectrum was scanned from 200 to 800 nm for pure BCZT and doped BCZT – xCo, as shown in Figure S2. The pure BCZT absorbs light at a wavelength below 400 nm, indicating absorption only UV light. However, after doping the BCZT – 0.02Co demonstrated a superior response in an extended range and exhibiting optical absorption. The band gap (E_g) of BCZT, BCZT - 0.01Co, BCZT - 0.015Co, BCZT - 0.02Co, and BCZT - 0.025Co was found to be E_g ~3.21, 2.90, 2.48, 2.40, 2.67 eV, respectively, as shown in Figure 3 (a-e). The band gap initially decreased with

increasing Co concentration, attaining a lowest bandgap at the composition $x = 0.02$, followed by an increase to $E_g \sim 2.67$ eV with a further substitution of Co to $x = 0.025$, as shown in Figure 3f. The oxygen vacancies created by Co ion substitution of Zr^{4+} or Ti^{4+} generated additional energy states near the top of the valence band and the bottom of the conduction band, leading to a decrease in band gap with an increase of Co doping and a resulting shift from the UV range to visible region [13]. However, when the Co doping level was increased to $x = 0.025$, the $BaCaTiO_4$ phase with a bandgap of $E_g \sim 3.14$ eV[45] could be precipitated, and its powder diffraction file (PDF) card is similar to that of $BaTiO_3$, leading to an increase in the band gap, as shown in Figure S3 and S4. After the incorporation of Co into the lattice of BCZT, the photocurrent is enhanced, as shown in Figure S5. Furthermore, compared with pure BCZT, the BCZT - *x*Co system exhibits a reduced band gap, which is promising for activation by visible light for photocatalytic reactions. However, the photocatalytic performance of BCZT-0.02Co is not significantly higher than that of pure BCZT, as shown in Figure S6. This may be due to the existence of defects caused by doping, those could act as electron-hole recombination centers[46].

3.3. Catalytic activity

Figure 4 shows that the catalytic activity of BCZT - *x*Co materials under different excitation conditions which were evaluated by the degradation of RhB. The BCZT - *x*Co powders were dispersed in a RhB solution, which was stirred in the dark. Subsequently, the RhB dye solution was used for photocatalytic reactions to characterise the catalytic performance of the BCZT - *x*Co ceramics. For comparison, and as a control, the self-degradation rate of RhB under the same conditions was also evaluated. The degradation rate ($D\%$) and the first-order kinetic rate constant (k) can be estimated from Equation (1) and (2) to determine the degradation performance.

$$Degradation\ rate(D\%) = [1 - (C_t/C_0)] \times 100\% \quad (1)$$

$$\ln(C_0/C_t) = kt \quad (2)$$

where t is reaction time, C_0 and C_t are the dye concentrations at time = *0* and t, respectively, and k can be evaluated through the ln (C_0/ C_t) − t plot to determine the kinetics of the degradation process. The trend of the kinetic curve is consistent with a linear fitting kinetic[47] and the resulting R^2 values are summarized in Table S1.

Figure 4a and 4b show the degradation efficiency and a ln (C_0/ C_t) − t plot when illuminated. A negligible adsorption of BCZT - 0.02Co is shown in Figure S7, which was stirred for 60 min in dark after reaching the adsorption-desorption equilibrium. The results confirm that the photocatalytic activity of BCZT-*x*Co ceramics are better than that of pure BCZT, which is consistent with the reduced band gap and transient photocurrent response, as shown in Figure 4 and S5. In particular, the photocatalytic of BCZT - 0.025Co is superior than that of BCZT - 0.02Co which has the lowest bandgap, and reasons for this will be discussed in Section 3.5.

Figure 4c and 4d show the piezocatalytic activity of the BCZT - *x*Co materials under ultrasonic vibration in the dark to explore the effect of Co doping on piezocatalytic performance. After achieving adsorption-desorption equilibrium, ultrasonication was selected to provide a periodic mechanical vibration. As shown in Figure 4(c), the degradation efficiencies of RhB were 77.1%, 75.0%, 72.8%, 69.9% and 63.4% respectively for pure BCZT, BCZT - 0.01Co, BCZT - 0.015Co, BCZT - 0.02Co and BCZT - 0.025Co under ultrasonic vibration for 60 min, indicating Co doping could decrease the piezocatalytic activity to some extent, which is in agreement with d_{33} data, as shown in Figure 2(b). It can be seen that the self-degradation efficiency of RhB, without any BCZT - *x*Co ceramic present, was negligible. To evaluate whether RhB degradation was due to sonocatalysis, a non-ferroelectric control sample was tested based on nanostructured Al_2O_3 and negligible RhB degradation was observed, as shown in Figure S8.

The performance under the application of both illumination and ultrasound are now examined. In Figure 4(e and f), the RhB degradation efficiencies were enhanced and reached 86.7%, 91.9%, 95.7%, 99.1% and 77.8% within 60 min under combined ultrasonic vibration and illumination for BCZT, BCZT - 0.01Co, BCZT - 0.015Co, BCZT - 0.02Co and BCZT - 0.025Co, respectively. A remarkable improvement can be observed during *combined* photo-piezo-catalysis for all samples when compared to piezocatalysis alone or photocatalysis alone. This large improvement suggests that the polarization-modulated built-in electric field in BCZT- *x*Co was beneficial for the separation and transfer of carriers[46], leading to the improved photo-piezo-catalytic activity of the doped BCZT - *x*Co materials.

The results have indicated that there is an appropriate level of doping of Co for superior photo-piezo-catalytic performance of BCZT - *x*Co. The RhB degradation kinetics of all samples were also investigated for illumination irradiation alone, ultrasonic vibration alone, and combined illumination/ultrasonic irradiation. The *k* data is summarized in Table 1, where it can be seen that the photo-piezo-catalytic performance of the BCZT - 0.02Co materials provided the best performance, and the *k* for combined photo-piezo-catalysis is higher than that of the sum of the individual illuminated and ultrasound conditions, indicating the strong degree of coupling between piezoelectricity and photoexcitation[48].

Figure 5(a) shows a comparison of the photocatalytic, piezocatalytic, and photo-piezo-catalytic degradation efficiency of the BCZT - *x*Co materials for 60 min. It can be seen that the degradation efficiencies of BCZT - 0.02Co for photocatalytic, piezocatalytic and photo-piezo-catalytic conditions are 21.6%, 69.9%, and 99.0% within 60 min, respectively. In addition, the first-order kinetic rate constant, *k*, for the BCZT - 0.02Co material under combined ultrasound and illumination conditions was 25 times and 4 times higher than those under illumination alone or under ultrasonic alone, as shown in Table 2. This enhancement indicates that the built-in electric field in the BCZT - *x*Co provided a driving force for the

separation and migration of electron-hole (e^--h^+) pairs[47]. Therefore, the piezoelectric properties of the BCZT - *x*Co materials is an important factor in improving its photocatalytic performance, which provides potential to broaden the application of piezoelectric materials in catalysis.

To compare the performance of photo-piezo-catalysts related to applications in pollution degradation, recent results in the literature and this work are summarized in Table 2; where the mechanism of the coupling effect between piezocatalysis and photocatalysis will be discussed in detail later.

3.4. Generated active species

Figure 5(b) shows the photo-piezo-catalytic degradation of RhB solution (C_0 = 10 mg/L), with and without the scavengers, where isopropyl alcohol (IPA), ethylenediaminetetraacetic acid (EDTA), and benzoquinone (BQ) were selected as specific scavengers for hydroxyl ion (·OH), photogenerated holes (h^+) and superoxide ($\cdot O_2^-$), respectively. The addition of EDTA decreased the degradation rate from 99% to 40%, implying that ·OH may have participated in the RhB degradation process. On adding IPA or BQ into the reaction solution, a large reduction in the degradation rate was observed, which indicated that $\cdot O_2^-$ and ·OH are the dominant active species for the photo-piezo-catalytic coupling effect.

Moreover, the exact active oxygen species ($\cdot O_2^-$ and ·OH) generated during piezocatalysis, photocatalysis, and photo-piezo-catalysis were verified by its electron spin resonance (ESR) spectrum; this is shown in Figure 5c and 5d, which is similar to those reports by Zheng et al.[47] and Liu et al.[49]. No signals of solvent were observed under the action of combined illumination and ultrasound. The BCZT - 0.02Co materials exhibited weak signals of both radicals under either ultrasonic or illumination, which could be considered as the contribution of piezocatalysis alone and photocatalysis alone. Stronger signals of both $\cdot O_2^-$ and ·OH for the BCZT - 0.02Co composition were detected under combined ultrasound and illumination, which is in agreement with the degradation results of RhB via piezocatalytic (ultrasound),

photocatalytic (light) and photo-piezo-catalytic (light and ultrasound) approaches. These results indicate the generation of $\cdot O_2^-$ and ·OH in the photo-piezo-catalytic system, which indicate the key role of the piezoelectric field during catalysis. The mechanism of photo-piezo-catalytic degradation can be represented as:

$$BCZT - xCo \xrightarrow{\text{light + ultrasound}} BCZT - xCo + h^+ + e^- \quad (3)$$

$$O_2 + e^- \rightarrow \cdot O_2^- \quad (4)$$

$$OH^- + h^+ \rightarrow \cdot OH \quad (5)$$

$$\cdot OH\ (or\ \cdot O_2^-) + \text{dye molecules} \rightarrow \text{dye decomposition} \quad (6)$$

3.5. Mechanism of photo-piezo-catalytic process

Figure 6 shows the Mott-Schottky data for the BCZT - *x*Co materials at different frequencies (i.e. 1kHz, 2kHz, and 3kHz, respectively) to reveal the energy band structures. The samples exhibit a positive slope on the Mott–Schottky plots, which indicated that they are an n-type semiconductor. Their flat-band potentials (V_{fb}) for BCZT - *x*Co (*x* = 0 - 0.025) were determined to be -0.53, -0.56, -0.59, -0.61 and -0.65 V (vs. Ag/AgCl) respectively, according to the x-intercepts of the plots. Since E(NHE) = E(Ag/AgCl) +0.197 eV [50], the conduction band (CB) position (E_{CB}) of BCZT, BCZT - 0.01Co, BCZT - 0.015Co, BCZT - 0.02Co, and BCZT - 0.025Co were -0.33, -0.36, -0.39, -0.41 and -0.45 eV (vs. NHE), respectively. A more negative E_{CB} indicates that the electrons on the conduction band of BCZT - 0.025Co possess a stronger capability for reducing O_2 to $\cdot O_2^-$ to decompose the RhB, resulting in the photocatalytic performance of BCZT - 0.025Co is superior to that of BCZT - 0.02Co; as shown in Figure 4a and 4b.

Since the band gap has been examined, the valence band (VB) position (E_{VB}) can be estimated according to $E_{VB} = E_{CB} + E_g$. Figure 7(a) shows a schematic energy band structure of pure BCZT and BCZT - 0.02Co. A schematic of the photo-piezo-catalytic process is also proposed, which is shown in Figure 7b

and 7c. As highlighted above, the $\cdot O_2^-$ and ·OH radicals play an important role in the catalytic activity, where the standard redox potentials of $O_2/\cdot O_2^-$ and $OH^-/\cdot OH$ are −0.33 eV and +1.90 eV versus NHE, respectively[51]. When there is no light or no ultrasound, the BCZT - 0.02Co powders remain in equilibrium with the solution at room temperature. The E_{VB} of BCZT - 0.02Co (+1.99 V vs. NHE) is more positive than the standard redox potential of $OH^-/\cdot OH$ to generate radicals. On the other hand, the E_{CB} of the BCZT - 0.02Co (−0.33 V vs. NHE) is more negative than the standard redox potential of $O_2/\cdot O_2^-$, thereby enabling the reduction of dissolved O_2 to generate radicals. In this case, the piezoelectric polarization (P_{piezo}) of the BCZT - 0.02Co corresponds to a minimum, as shown in Figure 7(a). Due to the high recombination rate, the concentration of free charges in BCZT - *x*Co is low, which lead to a low catalytic performance at this stage.

Figures 7b$_{1-3}$ shows the system when subjected to a periodic mechanical strain via the application of ultrasound for the piezocatalytic effect alone. The polarization of the piezoelectric particles (P_{piezo}) is changed by the ultrasound pressure over time during the catalytic process. Figure 7b$_1$ shows that when P_{piezo} is changed by a rising pressure, this can lead to the generation of positive-negative electric charges due to the piezoelectric effect[52] via Eq. (3). As a result, the temporary equilibrium of electric charges and associated screening charges is removed and space charges from the solution are adsorbed on the surface to balance the bound charges; this leaves charges in the electrolyte with opposite polarity to those being adsorbed to participate in the redox reactions for piezocatalytic dye degradation. On the cathode, electrons on the surface of the BCZT - *x*Co material attract the dissolved O_2 in the electrolyte and produce $\cdot O_2^-$ on the basis of Eq. (4). On the anode, $\cdot OH$ can be produced by positive charges (q^+) on the surface of BCZT - *x*Co on the basis of Eq. (5). Reactive species, such as $\cdot OH$ and $\cdot O_2^-$, are responsible for decomposing the organic molecules via Eq. (6). When P_{piezo} reaches a maximum value, this adsorption will disappear since

the bound charges are in a new equilibrium with screened charges, as shown in Figure 7b$_2$. Subsequently, the P_{piezo} falls to a minimum value and bound charges decrease, leading to the same level of piezocatalytic dye degradation again as shown in Figure 7b$_3$.

For combined photo-piezo-catalytic conditions, this coupling can also be described by four stages, as shown in Figures 7c$_{1-3}$. Unlike photocatalysis alone, piezocatalysis is now introduced, and the number of the charges increase sharply since the built-in electric field promotes charge separation and recombination of photoinduced charges [53]. As a result, the superior photo-piezo-catalytic activity of the BCZT - 0.02Co material is due to: (a) the increased number of generated electron-hole pairs as a result of the narrow bandgap, and (b) the built-in electric field of the ferroelectric material facilitates the separation of electron-hole pairs. This work demonstrates that doping in design of lead-free ferroelectric ceramics is of significant potential in the field of catalysis applications such as dye degradation, air purification and hydrogen production.

4. Conclusions

This work provides the first evaluation of the catalytic properties of ferroelectric ceramics based on $Ba_{0.85}Ca_{0.15}Zr_{0.1}(Ti_{1-x}Co_x)_{0.9}$ (BCZT - *x*Co, x = 0, 0.01 ,0.015, 0.02 and 0.025) prepared by a solid-state method. The BCZT - 0.02Co ceramic exhibited superior photo-piezo-catalytic properties for Rhodamine B (RhB) degradation, compared with pure BCZT, where the new material was able to fully degrade a RhB solution at an initial concentration (C_0) of 10 mg/L within 60 min, thereby demonstrating a high first order rate constant of $k \sim 0.081$ min^{-1}. The magnitude of the rate constant k for the BCZT - 0.02Co materials subjected to combined ultrasound and illumination was four times higher than when subjected to ultrasound alone and 25 times higher than illumination alone. Detailed characterisation and examination of the catalytic properties provided new insights into the mechanism by which the material acts as a catalyst,

where the enhanced photo-piezo-catalytic performance of the BCZT - 0.02Co materials was attributed to a combination of (i) a reduced band gap, which increased the amount of generated electron-hole pairs when illuminated and (ii) the built-in electric field of the active ferroelectric that facilitated charge carrier separation, thereby indicating a strong coupling between piezoelectricity and photoexcitation. This work therefore provides news ideas and directions for the design of functional materials with enhanced photo-piezo catalytic activity for dye degradation and other catalytic applications.

Declaration of Competing Interest

The authors declare that they have no known competing financial interests or personal relationships that could have appeared to influence the work reported in this paper.

Acknowledgment

The authors gratefully thank to the National Key R&D Program of China (No. 2022YFB3807400). This work was also supported by the Academy of Medical Sciences GCRF fund (GCRFNGR2-10059); Key Research and Development Project of Hunan Province (No. 2020WK2004); National Natural Science Foundation of China (Nos. U19A2087, 52002404, 52102150); The Leverhulme Trust (RGP-2018-290); and Overseas Talent Introduction Project of China.

References

[1] L. Zhang, W. Feng, B. Wang, K. Wang, F. Gao, Y. Zhao, P. Liu, Construction of dual-channel for optimizing Z-scheme photocatalytic system, Appl. Catal. B-Environ. 212 (2017) 80-88. https://doi.org/10.1016/j.apcatb.2017.04.049.

[2] H. Gong, L. Wang, K. Zhou, D. Zhang, Y. Zhang, V. Adamaki, A. Sergejevs, C. Bowen, Improved photocatalytic performance of gradient reduced TiO_2 ceramics with aligned pore channels, Adv. Powder Mater. 1 (2022) 100025. https://doi.org/10.1016/j.apmate.2021.11.011.

[3] H. You, Y. Jia, Z. Wu, X. Xu, W. Qian, Y. Xia, M. Ismail, Strong piezo-electrochemical effect of

multiferroic $BiFeO_3$ square micro-sheets for mechanocatalysis, Electrochem. Commun. 79 (2017) 55-58. https://doi.org/10.1016/j.elecom.2017.04.017.

[4] W.L. Yang, L. Zhang, J.F. Xie, X.D. Zhang, Q.H. Liu, T. Yao, S.Q. Wei, Q. Zhang, Y. Xie, Enhanced Photoexcited Carrier Separation in Oxygen-Doped $ZnIn_2S_4$ Nanosheets for Hydrogen Evolution, Angew. Chem.-Int. Edit. 55 (2016) 6716-6720. https://doi.org/10.1002/anie.201602543.

[5] L. Youssef, A.J.K. Leoga, S. Roualdes, J. Bassil, M. Zakhour, V. Rouessac, A. Ayral, M. Nakhl, Optimization of N-doped TiO_2 multifunctional thin layers by low frequency PECVD process, J. Eur. Ceram. Soc. 37 (2017) 5289-5303. https://doi.org/10.1016/j.jeurceramsoc.2017.05.010.

[6] Z. Wei, M. Janczarek, M. Endo, K. Wang, A. Balcytis, A. Nitta, M.G. Mendez-Medrano, C. Colbeau-Justin, S. Juodkazis, B. Ohtani, E. Kowalska, Noble metal-modified faceted anatase titania photocatalysts: Octahedron versus decahedron, Appl. Catal. B-Environ. 237 (2018) 574-587. https://doi.org/10.1016/j.apcatb.2018.06.027.

[7] Y. Zheng, X. Hou, Q. Li, Z. Fang, T. Yang, T. Liang, X. Duan, M. Shang, W. Yang, Electrostatic interaction assisted synthesis of a CdS/BCN heterostructure with enhanced photocatalytic effects, J. Mater. Chem. C. 8 (2020) 1803-1810. https://doi.org/10.1039/C9TC05896F.

[8] S. Li, M. Cai, Y. Liu, C. Wang, R. Yan, X. Chen, Constructing $Cd_{0.5}Zn_{0.5}S/Bi_2WO_6$ S-scheme heterojunction for boosted photocatalytic antibiotic oxidation and Cr (VI) reduction, Adv. Powder Mater. 2 (2023) 100073. https://doi.org/10.1016/j.apmate.2022.100073.

[9] W. Wu, Z.L. Wang, Piezotronics and piezo-phototronics for adaptive electronics and optoelectronics, Nat. Rev. Mater. 1 (2016) 1-17. https://doi.org/10.1038/natrevmats.2016.31.

[10] Y. Xue, T. Yang, Y.P. Zheng, E.H. Wang, H.Y. Wang, L.P. Zhu, Z.T. Du, X.M. Hou, K.C. Chou, The mechanism of a PVDF/CsPbBr3 perovskite composite fiber as a self-polarization piezoelectric nanogenerator with ultra-high output voltage, J. Mater. Chem. A. https://doi.org/10.1039/d2ta03559f.

[11] Z. Liang, C.F. Yan, S. Rtimi, J. Bandara, Piezoelectric materials for catalytic/photocatalytic removal of pollutants: Recent advances and outlook, Appl. Catal. B-Environ. 241 (2019) 256-269. https://doi.org/10.1016/j.apcatb.2018.09.028.

[12] K.P. Singh, G. Singh, R. Vaish, Utilizing the localized surface piezoelectricity of centrosymmetric $Sr_{1-x}Fe_xTiO_3$ (x <= 0.2) ceramics for piezocatalytic dye degradation, J. Eur. Ceram. Soc. 41 (2021) 326-334. https://doi.org/10.1016/j.eurceramsoc.2020.08.064.

[13] M. Sharma, R. Vaish, Piezo/pyro/photo-catalysis activities in $Ba_{0.85}Ca_{0.15}(Ti_{0.9}Zr_{0.1})(1-x)Fe_{(x)}O_{(3)}$ceramics, J. Am. Ceram. Soc. 104 (2021) 45-56. https://doi.org/10.1111/jace.17417.

[14] L. Zhou, T. Yang, L. Zhu, W. Li, S. Wang, X. Hou, X. Mao, Z.L. Wang, Piezoelectric nanogenerators with high performance against harsh conditions based on tunable N doped 4H-SiC nanowire arrays, Nano Energy. 83 (2021). https://doi.org/10.1016/j.nanoen.2021.105826.

[15] L. Zhou, L. Zhu, T. Yang, X. Hou, Z. Du, S. Cao, H. Wang, K.-C. Chou, Z.L. Wang, Ultra-Stable and Durable Piezoelectric Nanogenerator with All-Weather Service Capability Based on N Doped 4H-SiC Nanohole Arrays, Nano-Micro Letters. 14 (2022). https://doi.org/10.1007/s40820-021-00779-0.

[16] N. Setter, D. Damjanovic, L. Eng, G. Fox, S. Gevorgian, S. Hong, A. Kingon, H. Kohlstedt, N. Park, G. Stephenson, Ferroelectric thin films: Review of materials, properties, and applications, J. Appl. Phys. 100 (2006) 051606. https://doi.org/10.1063/1.2336999.

[17] H. Yang, Z. Wang, M. Sun, F. Chen, J. Ji, S. Chen, Y. Chen, D. Ma, Z. Zhang, B. Pan, Effect of pH, milling time, and Isobam content on porous silicon nitride ceramics prepared by gel casting, Adv. Powder Mater. 2 (2023) 100060.

[18] S.W. Xu, W.Q. Qian, D. Zhang, X. Zhao, X.M. Zhang, C.B. Li, C.R. Bowen, Y. Yang, A coupled photo-

piezo-catalytic effect in a BST-PDMS porous foam for enhanced dye wastewater degradation, Nano Energy. 77 (2020) 105305-105315. https://doi.org/10.1016/j.nanoen.2020.105305.

[19] Y. Bai, J. Zhao, Z. Lv, K. Lu, Enhanced piezo-phototronic effect of ZnO nanorod arrays for harvesting low mechanical energy, Ceram. Int. 45 (2019) 15065-15072. https://doi.org/10.1016/j.ceramint.2019.04.243.

[20] S. Kumar, M. Sharma, A. Kumar, S. Powar, R. Vaish, Rapid bacterial disinfection using low frequency piezocatalysis effect, J. Ind. Eng. Chem. 77 (2019) 355-364. https://doi.org/10.1016/j.jiec.2019.04.058.

[21] M. Sharma, G. Singh, R. Vaish, Dye degradation and bacterial disinfection using multicatalytic $BaZr_{0.02}Ti_{0.98}O_3$ ceramics, J. Am. Ceram. Soc. 103 (2020) 4774-4784. https://doi.org/10.1111/jace.17171.

[22] M. Lun, X. Zhou, S. Hu, Y. Hong, B. Wang, A. Yao, W. Li, B. Chu, Q. He, J. Cheng, Y. Wang, Ferroelectric $K_{0.5}Na_{0.5}NbO_3$ catalysts for dye wastewater degradation, Ceram. Int. 47 (2021) 28797-28805. https://doi.org/10.1016/j.ceramint.2021.07.040.

[23] E. Lin, J. Wu, N. Qin, B. Yuan, Z. Kang, D. Bao, Enhanced piezocatalytic, photocatalytic and piezo-/photocatalytic performance of diphasic $Ba_{1-x}Ca_xTiO_3$ nanowires near a solubility limit, Catal. Sci. Technol. 9 (2019) 6863-6874. https://doi.org/10.1039/c9cy01713e.

[24] W. Liu, X. Ren, Large Piezoelectric Effect in Pb-Free Ceramics, Phys.rev.lett. 103 (2009) 257602. https://doi.org/10.1103/PhysRevLett.103.257602.

[25] D. Xue, Y. Zhou, H. Bao, J. Gao, C. Zhou, X. Ren, Large piezoelectric effect in Pb-free Ba (Ti, Sn) O_3-x (Ba, ca) TiO_3 ceramics, Appl. Phys. Lett. 99 (2011) 122901. https://doi.org/10.1063/1.3640214.

[26] A.B. Haugen, J.S. Forrester, D. Damjanovic, B. Li, K.J. Bowman, J.L. Jones, Structure and phase transitions in $0.5(Ba_{0.7}Ca_{0.3}TiO_3)$-$0.5(BaZr_{0.2}Ti_{0.8}O_3)$ from -100 degrees C to 150 degrees C, J. Appl. Phys. 113 (2013) 1-6. https://doi.org/10.1063/1.4772741.

[27] R.P. Tiwari, V. Kumar, S. Singh, J. Shah, R.K. Kotnala, B. Birajdar, Structural phase transition, impedance spectroscopy and narrow optical band Gap in (1-x)$KNbO_3$-x $Ba(Sc_{1/2}Nb_{1/2})$ O_3, J. Eur. Ceram. Soc. 38 (2018) 1427-1433. https://doi.org/10.1016/j.jeurceramsoc.2017.12.015.

[28] Y.M. Zhang, H.M. Deng, S.F. Si, T.T. Wang, D.L. Zheng, P.X. Yang, J.H. Chu, Band gap narrowing and magnetic properties of transition-metal-doped $Ba_{0.85}Ca_{0.15}Ti_{0.9}Zr_{0.1}O3$ lead-free ceramics, J. Am. Ceram. Soc. 103 (2020) 2491-2498. https://doi.org/10.1111/jace.16924.

[29] Q. Liu, D. Zhai, Z. Xiao, C. Tang, Q. Sun, C.R. Bowen, H. Luo, D. Zhang, Piezo-photoelectronic coupling effect of $BaTiO_3$@TiO_2 nanowires for highly concentrated dye degradation, Nano Energy. 92 (2022) 1-14. https://doi.org/10.1016/j.nanoen.2021.106702.

[30] M. Sharma, T. Singhal, R. Vaish, Effect of ferroelectric polarization on piezo/photocatalysis in Ag nanoparticles loaded $0.5(Ba_{0.7}Ca_{0.3})TiO_3$-$0.5Ba(Zr_{0.1}Ti_{0.9})O_{-3}$ composites towards the degradation of organic pollutants, J. Am. Ceram. Soc. 105 (2021) 3165-3176. https://doi.org/10.1111/jace.18298.

[31] R.T. Asahi, T. Morikawa, T. Ohwaki, K. Aoki, Y. Taga, Visible-Light Photocatalysis in Nitrogen-Doped Titanium Oxides, Science. 293 (2001) 269-271. https://doi.org/10.1126/science.1061051.

[32] S. Samanta, M. Rath, V. Sankaranarayanan, K. Sethupathi, M.S.R. Rao, Effective Bandgap Engineering in Perovskite Ferroelectrics by Successive Multiple Doping, Phys. Status Solidi B-Basic Solid State Phys. 257 (2020) 1-7. https://doi.org/10.1002/pssb.201900272.

[33] S.F. Shi, H. Hashimoto, T. Sekino, Enhancing piezoelectric properties of $Ba_{0.88}Ca_{0.12}Zr_{0.12}Ti_{0.88}O_3$ lead-free ceramics by doping Co ions, Ceram. Int. 47 (2021) 3272-3278. https://doi.org/10.1016/j.ceramint.2020.09.167.

[34] C. Pascual-Gonzalez, G. Schileo, A. Khesro, I. Sterianou, D.W. Wang, I.M. Reaney, A. Feteira, Band gap evolution and a piezoelectric-to-electrostrictive crossover in (1-x)KNbO3-x$(Ba_{0.5}Bi_{0.5})(Nb_{0.5}Zn_{0.5})O_{-3}$

ceramics, J. Mater. Chem. C. 5 (2017) 1990-1996. https://doi.org/10.1039/c6tc05515j.
[35] B. Liu, Y. Zhang, L. Tang, X-ray photoelectron spectroscopic studies of $Ba_{0.5}Sr_{0.5}Co_{0.8}Fe_{0.2}O_{3-\delta}$ cathode for solid oxide fuel cells, Int. J. Hydrog. Energy. 34 (2009) 435-439. https://doi.org/10.1016/j.ijhydene.2008.10.046.
[36] P. Jaimeewong, S. Sittinon, S. Buntham, P. Bomlai, O. Namsar, S. Pojprapai, A. Watcharapasorn, Ferroelectric, Piezoelectric and Dielectric Behaviors of CoO- and Fe_2O_3-Doped BCZT Ceramics, Phys. Status Solidi A-Appl. Mat. 215 (2018) 1-6. https://doi.org/10.1002/pssa.201701023.
[37] S.P.P. Sadhu, S. Siddabattuni, V.S. Muthukumar, K.B.R. Varma, Enhanced dielectric properties and energy storage density of surface engineered BCZT/PVDF-HFP nanodielectrics, J. Mater. Sci.-Mater. Electron. 29 (2018) 6174-6182. https://doi.org/10.1007/s10854-018-8592-4.
[38] R.D. Shannon, Revised effective ionic radii and systematic studies of interatomic distances in halides and chalcogenides, Acta Crystallogr. Sect. A. 32 (1976) 751-767. https://doi.org/10.1107/S0567739476001551.
[39] A. Ms, A. Jd, C.A. Chong, F.A. Peng, L.A. Peng, A. Jh, B. Zy, L.A. Wei, Enhanced piezoelectric properties in M (M = Co or Zn)-doped $Ba_{0.99}Ca_{0.01}Ti_{0.98}Zr_{0.02}O_3$ ceramics, Ceram. Int. 46 (2020) 17351-17360. https://doi.org/10.1016/j.ceramint.2020.04.024.
[40] E.V. Ramana, F. Figueiras, A. Mahajan, D.M. Tobaldi, B.F.O. Costa, M.P.F. Graca, M.A. Valente, Effect of Fe-doping on the structure and magnetoelectric properties of $(Ba_{0.85}Ca_{0.15})(Ti_{0.9}Zr_{0.1})O_{-3}$ synthesized by a chemical route, J. Mater. Chem. C. 4 (2016) 1066-1079. https://doi.org/10.1039/c5tc00914f.
[41] J.H. Park, H.M. Jang, H.S. Kim, C.G. Park, S.G. Lee, Strain-mediated magnetoelectric coupling in $BaTiO_3$-Co nanocomposite thin films, Appl. Phys. Lett. 92 (2008) 1-4. https://doi.org/10.1063/1.2842383.
[42] W. Zhou, H. Deng, L. Yu, P. Yang, J. Chu, Magnetism switching and band-gap narrowing in Ni-doped $PbTiO_3$ thin films, J. Appl. Phys. 117 (2015) 1-6. https://doi.org/10.1063/1.4921459.
[43] M.Z. Gao, W.W. Ge, X. Li, H.M. Yuan, C.Y. Liu, H.W. Zhao, Y.Q. Ma, Y.F. Chang, Enhanced Dielectric and Energy Storage Properties in Fe-Doped BCZT Ferroelectric Ceramics, Phys. Status Solidi A-Appl. Mat. 217 (2020) 1-5. https://doi.org/10.1002/pssa.202000253.
[44] A. Dolgonos, T.O. Mason, K.R. Poeppelmeier, Direct optical band gap measurement in polycrystalline semiconductors: A critical look at the Tauc method, J. Solid State Chem. 240 (2016) 43-48. https://doi.org/10.1016/j.jssc.2016.05.010.
[45] R. Muhammad, M.A. Khalil, M.S. Castro, Structure and dielectric characteristics of $Ba_{1-x}Ca_xTi_{1-x}Ca_xO_{3-\delta}$ ceramics, Ceram. Int. 46 (2020) 1059-1064. https://doi.org/10.1016/j.ceramint.2019.09.072.
[46] J. Yuan, X. Huang, L. Zhang, F. Gao, R. Lei, C. Jiang, W. Feng, P. Liu, Tuning piezoelectric field for optimizing the coupling effect of piezo-photocatalysis, Appl. Catal. B-Environ. 278 (2020) 119291. https://doi.org/10.1016/j.apcatb.2020.119291.
[47] H. Zheng, X. Li, K. Zhu, P. Liang, M. Wu, Y. Rao, R. Jian, F. Shi, J. Wang, K. Yan, J. Liu, Semiconducting $BaTiO_3$@C core-shell structure for improving piezo-photocatalytic performance, Nano Energy. 93 (2022) 1-13. https://doi.org/10.1016/j.nanoen.2021.106831.
[48] R. Wang, X. Xie, C. Xu, Y. Lin, D. You, J. Chen, Z. Li, Z. Shi, Q. Cui, M. Wang, Bi-piezoelectric effect assisted ZnO nanorods/PVDF-HFP spongy photocatalyst for enhanced performance on degrading organic pollutant, Chem. Eng. J. 439 (2022). https://doi.org/10.1016/j.cej.2022.135787.
[49] Q. Liu, F. Zhan, H. Luo, D. Zhai, Z. Xiao, Q. Sun, Q. Yi, Y. Yang, D. Zhang, Mechanism of interface engineering for ultrahigh piezo-photoelectric catalytic coupling effect of $BaTiO_3$@ TiO_2 microflowers, Appl. Catal. B-Environ. 318 (2022) 121817. https://doi.org/10.1016/j.apcatb.2022.121817.

[50] M.X. Song, K.M. Qi, Y. Wen, X.L. Zhang, Y. Yuan, X.Y. Xie, Z.W. Wang, Rational design of novel three-dimensional reticulated Ag_2O/ZnO Z-scheme heterojunction on Ni foam for promising practical photocatalysis, Sci. Total Environ. 793 (2021) 1-13. https://doi.org/10.1016/j.scitotenv.2021.148519.
[51] P. Wardman, Reduction potentials of one-electron couples involving free radicals in aqueous solution, J. Phys. Chem. Ref. Data. 18 (1989) 1637-1755. https://doi.org/10.1063/1.555843.
[52] K.-S. Hong, H. Xu, H. Konishi, X. Li, Piezoelectrochemical effect: a new mechanism for azo dye decolorization in aqueous solution through vibrating piezoelectric microfibers, J. Phys. Chem. C. 116 (2012) 13045-13051. https://doi.org/10.1021/jp211455z.
[53] K. Wang, C. Han, J. Li, J. Qiu, J. Sunarso, S. Liu, The Mechanism of Piezocatalysis: Energy Band Theory or Screening Charge Effect?, Angew. Chem.-Int. Edit. (2021) 1-13. https://doi.org/10.1002/anie.202110429.
[54] D.F. Yu, Z.H. Liu, J.M. Zhang, S. Li, Z.C. Zhao, L.F. Zhu, W.S. Liu, Y.H. Lin, H. Liu, Z.T. Zhang, Enhanced catalytic performance by multi-field coupling in $KNbO_3$ nanostructures: Piezo-photocatalytic and ferro-photoelectrochemical effects, Nano Energy. 58 (2019) 695-705. https://doi.org/10.1016/j.nanoen.2019.01.095.
[55] A. Sharma, U. Bhardwaj, H.S. Kushwaha, ZnO hollow pitchfork: coupled photo-piezocatalytic mechanism for antibiotic and pesticide elimination, Catal. Sci. Technol. 12 (2022) 812-822. https://doi.org/10.1039/d1cy01973b.
[56] X.Y. Jiang, H.R. Wang, X. Wang, G.L. Yuan, Synergetic effect of piezoelectricity and Ag deposition on photocatalytic performance of barium titanate perovskite, Sol. Energy. 224 (2021) 455-461. https://doi.org/10.1016/j.solener.2021.06.032.
[57] X. Zhou, Q. Sun, D. Zhai, G. Xue, H. Luo, D. Zhang, Excellent catalytic performance of molten-salt-synthesized $Bi_{0.5}Na_{0.5}TiO_3$ nanorods by the piezo-phototronic coupling effect, Nano Energy. 84 (2021) 1-12. https://doi.org/10.1016/j.nanoen.2021.105936.
[58] H. Lei, H.H. Zhang, Y. Zou, X.P. Dong, Y.M. Jia, F.F. Wang, Synergetic photocatalysis/piezocatalysis of bismuth oxybromide for degradation of organic pollutants, J. Alloy. Compd. 809 (2019) 1-6. https://doi.org/10.1016/j.jallcom.2019.151840.
[59] Z.C. Zhao, L.Y. Wei, S. Li, L.F. Zhu, Y.P. Su, Y. Liu, Y.B. Bu, Y.H. Lin, W.S. Liu, Z.T. Zhang, Exclusive enhancement of catalytic activity in $Bi_{0.5}Na_{0.5}TiO_3$ nanostructures: new insights into the design of efficient piezocatalysts and piezophotocatalysts, J. Mater. Chem. A. 8 (2020) 16238-16245. https://doi.org/10.1039/c9ta14007g.

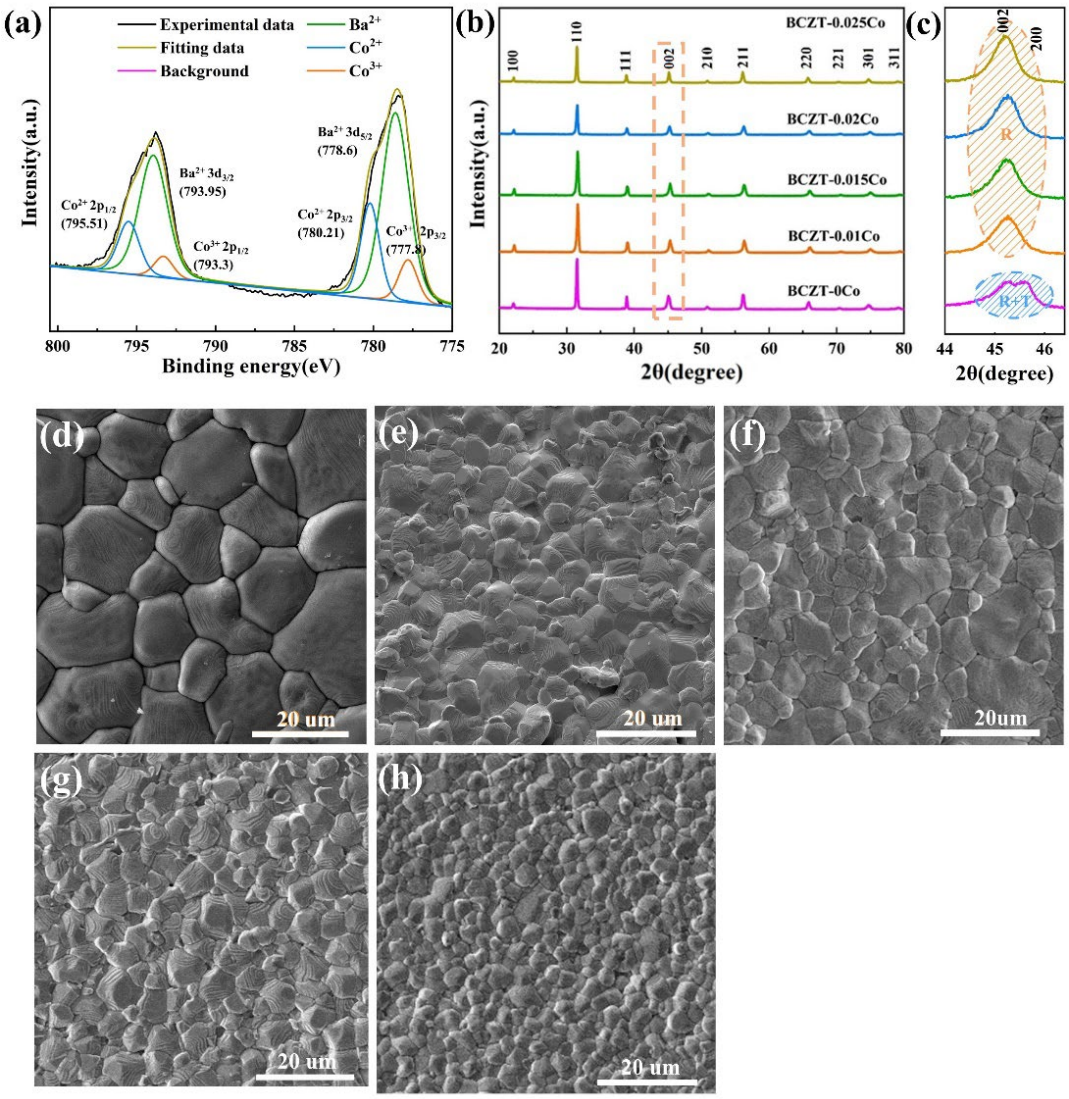

Figure 1 (a) XPS of Co 2p and Ba 3d of the BCZT - *x*Co powders at *x* = 0.02. (b) XRD patterns and (c) expanded XRD patterns of BCZT - *x*Co powders. SEM images of sintered BCZT - *x*Co materials: (d) *x* = 0; (e) *x* = 0.01; (f) *x* = 0.015; (g) *x* = 0.02; (h) *x* = 0.025.

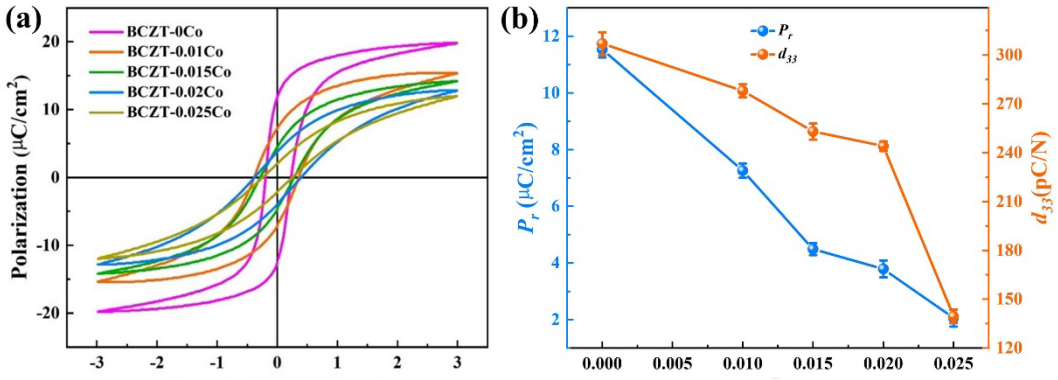

Figure 2 (a) Ferroelectric polarisation – electric field hysteresis loops, (b) remnant polarization (P_r) and piezoelectric coefficient (d_{33}) of the BCZT - xCo materials.

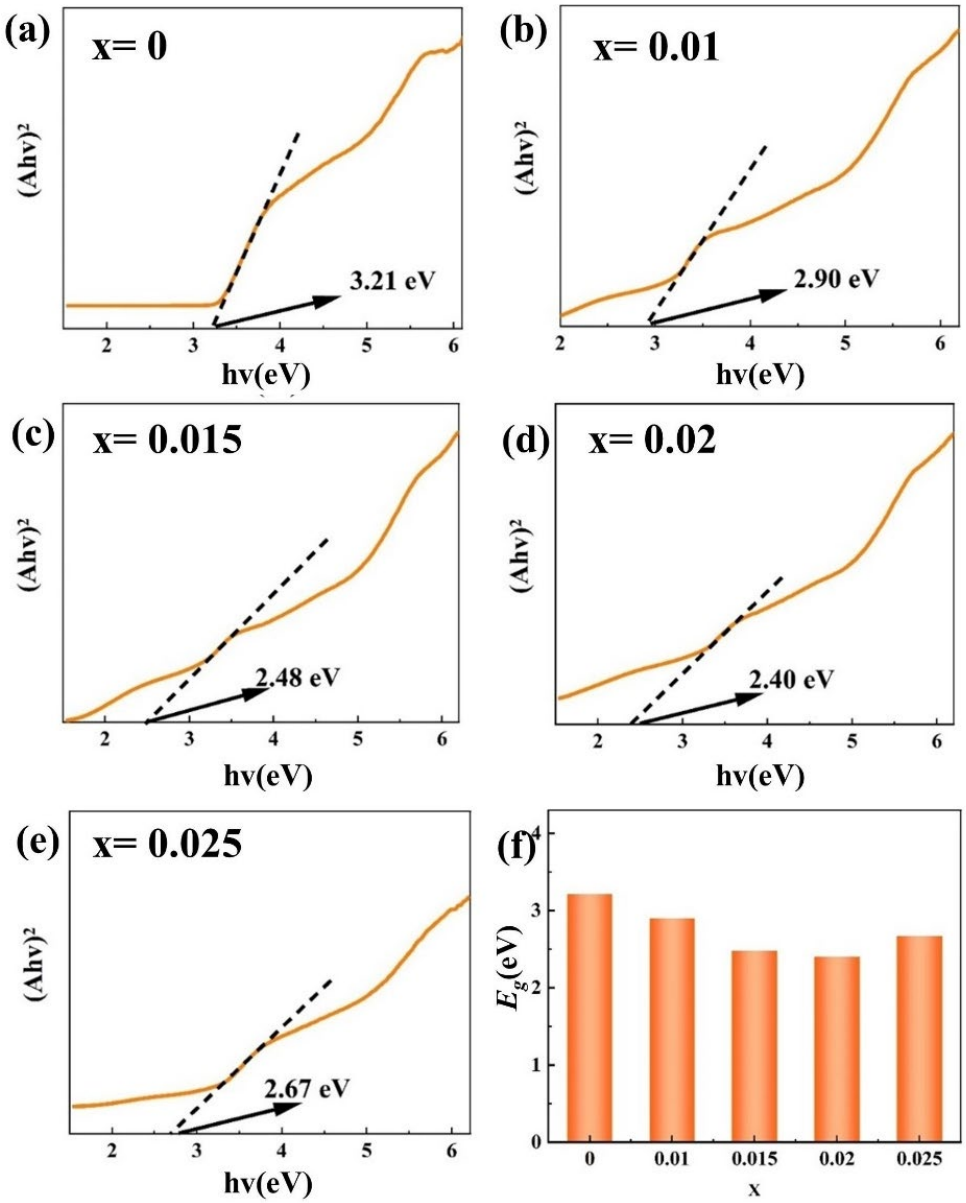

Figure 3 Band gaps of BCZT - *x*Co: (a) $x = 0$; (b) $x = 0.01$; (c) $x = 0.015$; (d) $x = 0.02$; (e) $x = 0.025$, (f) relationship between Co addition (x) and optical band gap.

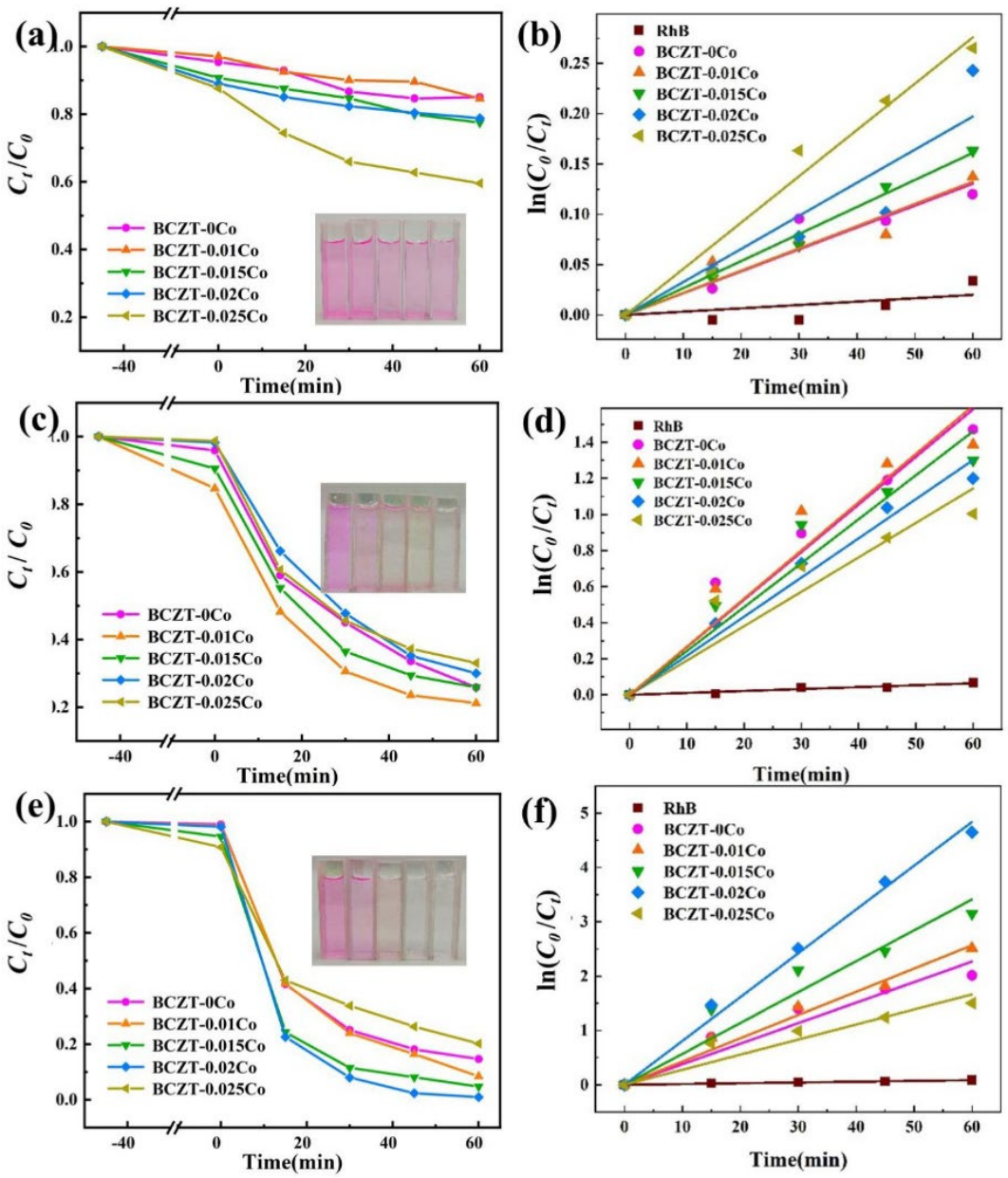

Figure 4 Catalytic activity of BCZT - *x*Co under different conditions: (a) photocatalytic degradation efficiency and (b) fitting of kinetic curves; (c) piezo-catalytic degradation efficiency and (d) fitting of kinetic curves; (e) photo-piezo-catalytic degradation efficiency and (f) fitting of kinetic curves. Inset of images represents the concentration change of RhB with BCZT - 0.02Co. Inset shows the colour change of the RhB dye solution with increasing reaction time.

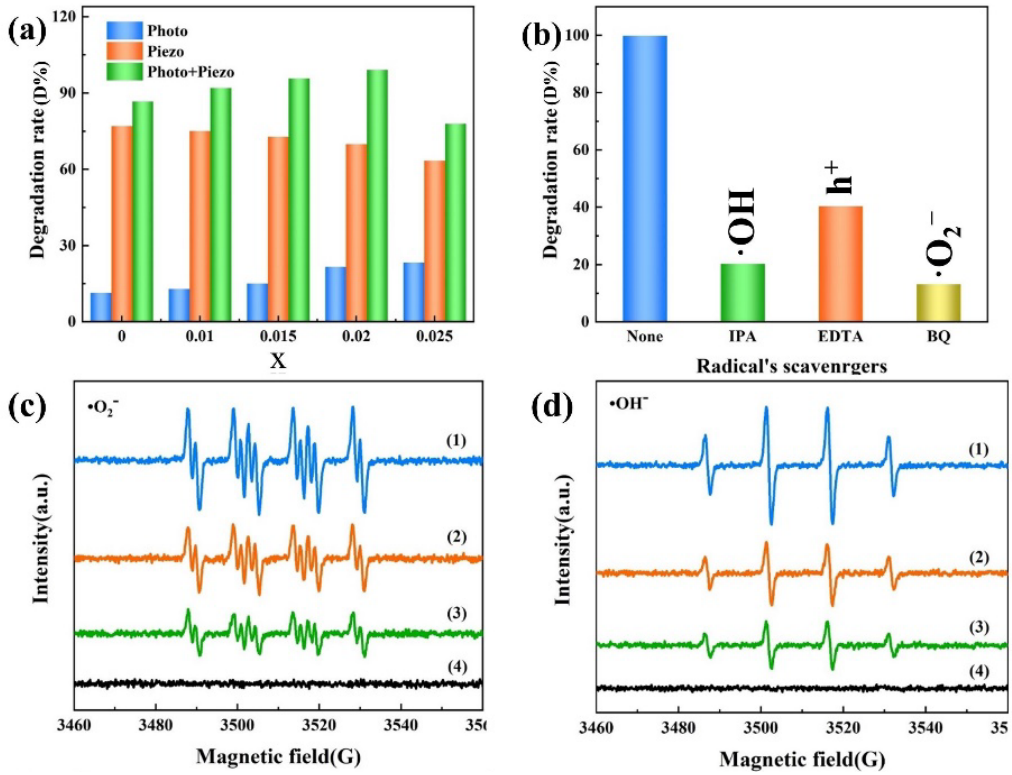

Figure 5 (a) Degradation for BCZT - *x*Co ceramics. (b) Effect of various scavengers during photo-piezocatalysis for the BCZT - 0.02Co ceramics. ESR of (c) $\cdot O_2^-$ and (d) ·OH with radical spin-trapped by DMPO over (1) BCZT - 0.02Co + illumination + ultrasound; (2) BCZT - 0.02Co + ultrasound; (3) BCZT - 0.02Co + illumination and (4) solvent + illumination + ultrasound, respectively.

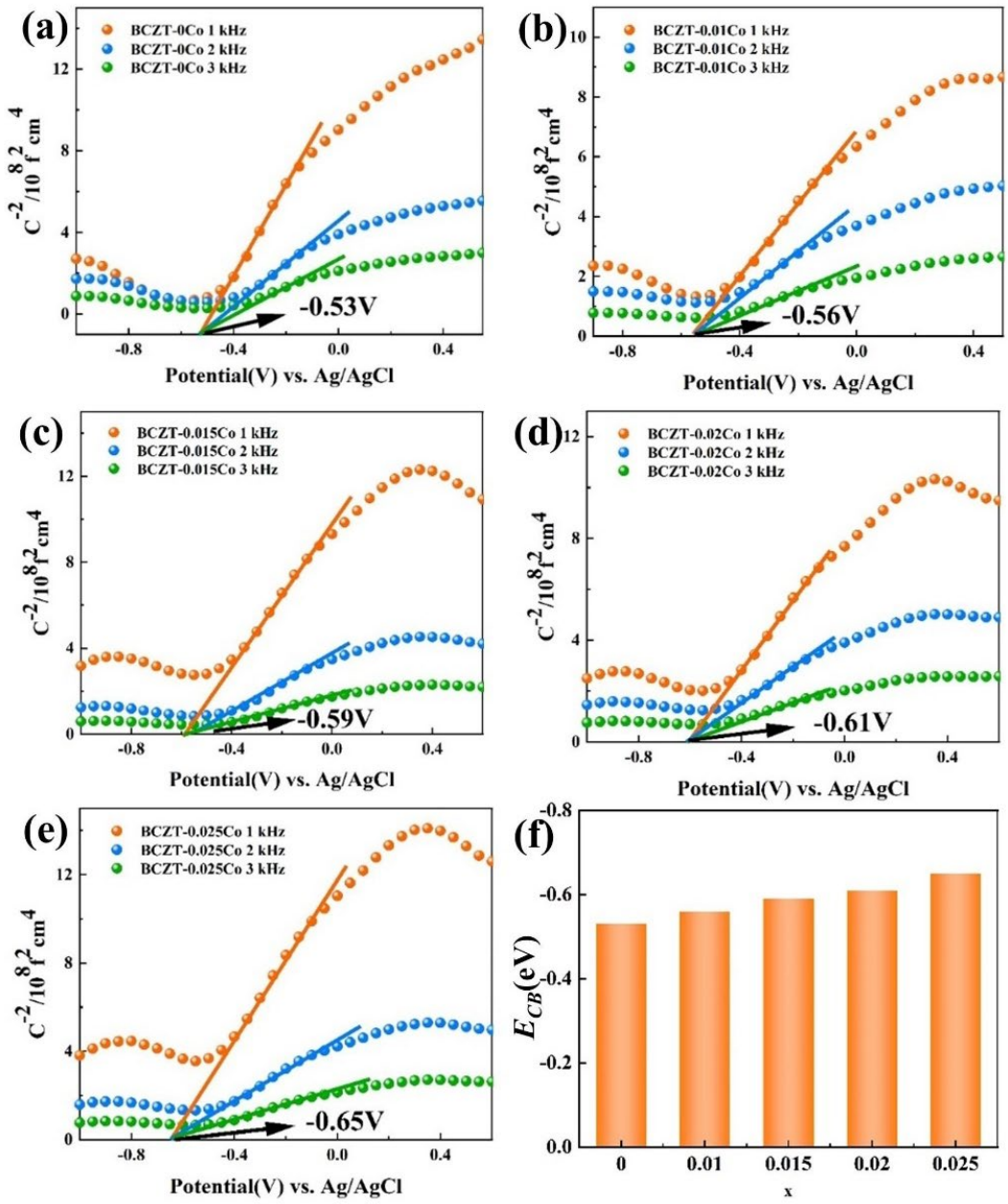

Figure 6 Mott-Schottky plots of BCZT - *x*Co powders: (a) $x = 0$; (b) $x = 0.01$; (c) $x = 0.015$; (d) $x = 0.02$; (e) $x = 0.025$ at different frequencies, (f) relationship between Co addition x and E_{CB}.

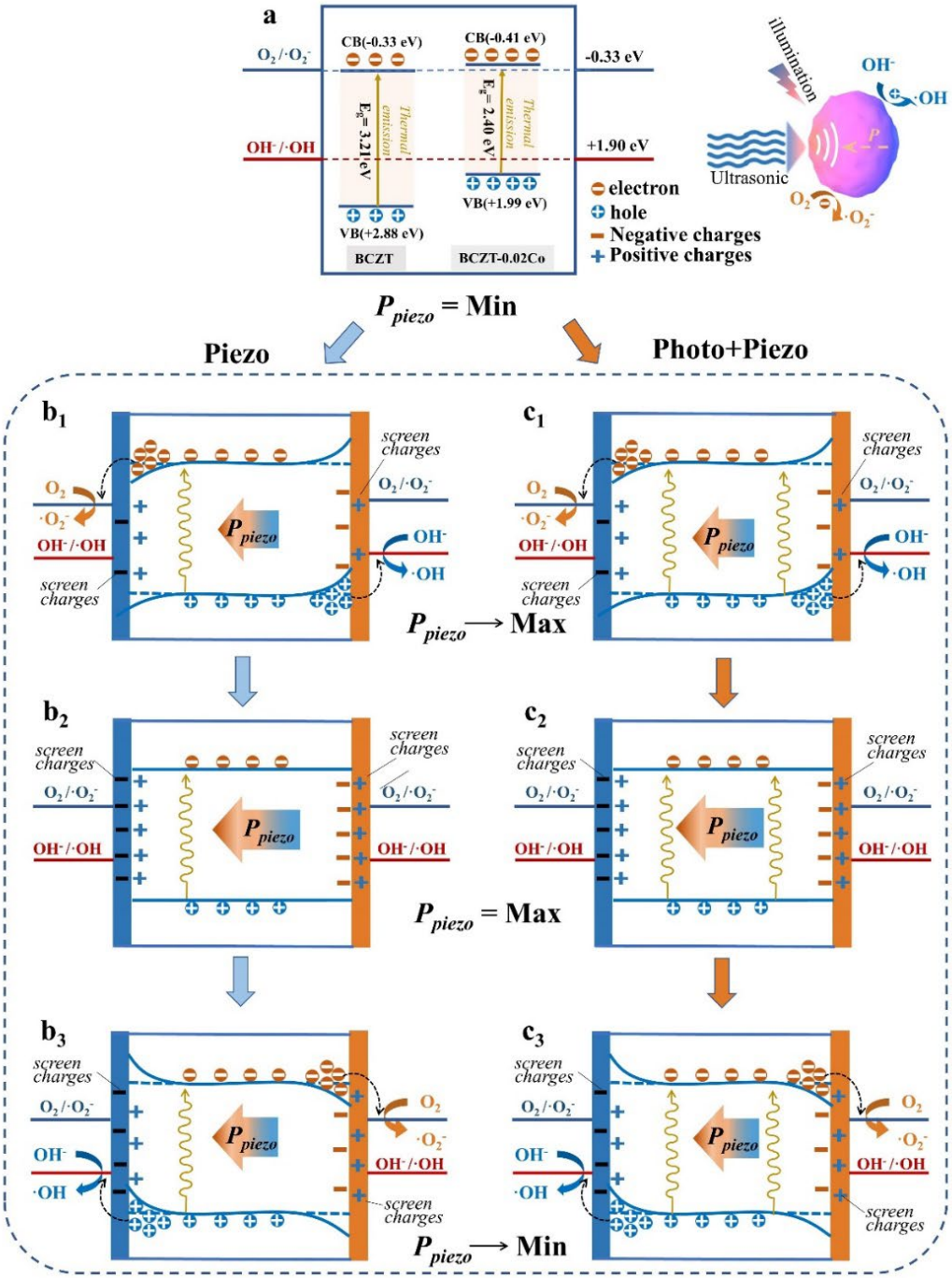

Figure 7 (a) Schematic of energy band structures of BCZT and BCZT - 0.02Co in equilibrium with the solution. ($b_{1\text{-}3}$) Energy band structure of BCZT - 0.02Co during piezocatalysis. ($c_{1\text{-}3}$) Energy band structure of BCZT - 0.02Co during photo-piezo-catalysis, where P_{piezo} is polarization of the piezoelectric particles.

Table 1

First-order kinetic rate constant (k) for the photocatalytic, piezocatalytic and photo-piezo-catalytic activity of BCZT – xCo

Activity	first-order kinetic rate constant	BCZT - 0Co	BCZT - 0.01Co	BCZT - 0.015Co	BCZT - 0.02Co	BCZT - 0.025Co
Photo	k x 10^3 min^{-1}	2.2	2.2	2.7	3.3	4.6
Piezo	k x 10^3 min^{-1}	26.4	26.7	24.3	21.7	19.1
Photo-piezo	k x 10^3 min^{-1}	37.8	42.8	56.8	80.6	27.7

Table 2

First-order kinetic rate constant, k values, recently reported for photo-piezo-catalysts.

Catalyst	C (Catalyst)(g/L)	C (Dye)	Condition	k × 10^{-3} (min^{-1})	Ref.
$KNbO_3$ nanosheets	0.5	10mg/L RhB	Ultrasound:40 kHz, 110 W Light: 300 W	22	[54]
ZnO hollow pitchfork	1.0	10mg/L RhB	Ultrasound:40 kHz, 120 W Light: 100 W	22.9	[55]
Ag deposited $BaTiO_3$ nanopowders	1.0	5mg/L RhB	Ultrasound: 150 W Light: 500 W	22.3	[56]
BNT nanorods	1.0	5mg/L RhB	Ultrasound: 28 kHz, 200 W Light:300 W	94	[57]
$BaTiO_3$@C core-shell	1.0	10mg/L RhB	Ultrasound: 40 kHz, 120 W Light:300 W	35.9	[47]
BiOBr nanoflakes	1.0	10 mg/L RhB	Ultrasound:40 kHz, 120 W Light: 9 W	71	[58]
BNT nanospheres	0.5	10mg/L RhB	Ultrasound: 40 kHz, 110 W Light: 300W	61	[59]
KNN particles	1.0	5 mg/L RhB	Ultrasound: 40 kHz, Light: 350W	39.7	[22]

BCZT-0Co	1.0	10mg/L RhB	Ultrasound: 45 kHz, 200 W Light: 300W	37.8	This work
BCZT-0.02Co	1.0	10mg/L RhB	Ultrasound: 45 kHz, 200 W Light: 300W	80.6	This work